



Design of perovskite/crystalline-silicon monolithic tandem solar cells

S. ALTAZIN,^{1,*} L. STEPANOVA,¹ J. WERNER,² B. NIESEN,² C. BALLIF,² AND B. RUHSTALLER^{1,3}

¹Fluxim AG, Katharina-Sulzer-Platz 2, 8400 Winterthur, Switzerland

²Photovoltaics and Thin-Film Electronics Laboratory, Institute of Microengineering (IMT), Ecole Polytechnique Fédérale de Lausanne (EPFL), Rue de la Maladière 71 b, 2002 Neuchâtel, Switzerland

³Zurich University of Applied Sciences, Institute of Computational Physics, Wildbachstrasse 21, 8401 Winterthur, Switzerland

*beat.ruhstaller@fluxim.com

Abstract: We present an optical model implemented in the commercial software SETFOS 4.6 for simulating perovskite/silicon monolithic tandem solar cells that exploit light scattering structures. In a first step we validate the model with experimental data of tandem solar cells that either use front- or rear-side textures and extract the internal quantum efficiency of the methyl-ammonium lead iodide (MALI) perovskite sub-cell. In a next step, the software is used to investigate the potential of different device architectures featuring a monolithic integration between the perovskite and silicon sub-cells and exploiting rear- as well as front-side textures for improved light harvesting. We find that, considering the available contact materials, the *p-i-n* solar cell architecture is the most promising with respect to achievable photocurrent for both flat and textured wafers. Finally, cesium-formamidinium-based perovskite materials with several bandgaps were synthesized, optically characterized and their potential in a tandem device was quantified by simulations. For the simulated layer stack and among the tested materials with bandgaps of 1.7 and 1.6 eV, the one with 1.6 eV bandgap was found to be the most promising, with a potential of reaching a power conversion efficiency of 31%. In order to achieve higher efficiencies using higher band-gap materials, parasitic absorbance in the blue spectral range should be further reduced.

© 2018 Optical Society of America under the terms of the [OSA Open Access Publishing Agreement](#)

OCIS codes: (040.5350) Photovoltaic; (350.6050) Solar energy.

References and links

1. K. Yoshikawa, H. Kawasaki, W. Yoshida, T. Irie, K. Konishi, K. Nakano, T. Uto, D. Adachi, M. Kanematsu, H. Uzu, and K. Yamamoto, "Silicon heterojunction solar cell with interdigitated back contacts for a photoconversion efficiency over 26%," *Nat. Energy* **2**(5), 17032 (2017).
2. J. Werner, B. Niesen, and C. Ballif, "Perovskite/Silicon Tandem Solar Cells: Marriage of Convenience or True Love Story? - An Overview," *Adv. Mater. Interfaces* **5**(1), 1700731 (2018).
3. K. A. Bush, A. F. Palmstrom, Z. J. Yu, M. Boccard, R. Cheacharoen, J. P. Mailoa, D. P. McMeekin, R. L. Z. Hoye, C. D. Bailie, T. Leijtens, I. M. Peters, M. C. Minichetti, N. Rolston, R. Prasanna, S. Sofia, D. Harwood, W. Ma, F. Moghadam, H. J. Snaith, T. Buonassisi, Z. C. Holman, S. F. Bent, and M. D. McGehee, "23.6%-efficient monolithic perovskite/silicon tandem solar cells with improved stability," *Nat. Energy* **2**(4), 17009 (2017).
4. T. Duong, Y. L. Wu, H. Shen, J. Peng, X. Fu, D. Jacobs, E. C. Wang, T. C. Kho, K. C. Fong, M. Stocks, E. Franklin, A. Blakers, N. Zin, K. McIntosh, W. Li, Y. B. Cheng, T. P. White, K. Weber, and K. Catchpole, "Rubidium Multication Perovskite with Optimized Bandgap for Perovskite-Silicon Tandem with over 26% Efficiency," *Adv. Energy Mater.* **7**(14), 1–11 (2017).
5. C. O. Ramírez Quiroz, Y. Shen, M. Salvador, K. Forberich, N. Schrenker, G. D. Spyropoulos, T. Heumüller, B. Wilkinson, T. Kirchartz, E. Spiecker, P. J. Verlinden, X. Zhang, M. A. Green, A. Ho-Baillie, and C. J. Brabec, "Balancing electrical and optical losses for efficient 4-terminal Si-perovskite solar cells with solution processed percolation electrodes," *J. Mater. Chem. A Mater. Energy Sustain.* **6**(8), 3583–3592 (2018).
6. S. Albrecht, M. Saliba, J.-P. Correa-Baena, K. Jäger, L. Korte, A. Hagfeldt, M. Grätzel, and B. Rech, "Towards optical optimization of planar monolithic perovskite/silicon-heterojunction tandem solar cells," *J. Opt.* **18**(6), 64012 (2016).
7. D. T. Grant, K. R. Catchpole, K. J. Weber, and T. P. White, "Design guidelines for perovskite/silicon 2-terminal tandem solar cells: an optical study," *Opt. Express* **24**(22), A1454–A1470 (2016).

8. R. Santbergen, R. Mishima, T. Meguro, M. Hino, H. Uzu, J. Blanker, K. Yamamoto, and M. Zeman, "Minimizing optical losses in monolithic perovskite/c-Si tandem solar cells with a flat top cell," *Opt. Express* **24**(18), A1288–A1299 (2016).
9. D. Chen, P. Manley, P. Tockhorn, D. Eisenhauer, G. Köppel, M. Hammerschmidt, S. Burger, S. Albrecht, C. Becker, and K. Jäger, "Nanophotonic light management for perovskite–silicon tandem solar cells," *J. Photonics Energy* **8**(02), 1 (2018).
10. H. Chung, R. Singh, L. Kumar, M. A. Alam, and P. Bermel, "Characterization and redesign of perovskite/silicon tandem cells," in *Conf. Rec. IEEE Photovolt. Spec. Conf.* (2016), pp. 3625–3628.
11. S. Altazin, L. Stepanova, K. Lapagna, P. Losio, J. Werner, B. Niesen, A. Dabirian, M. Morales-Masis, S. De Wolf, C. Ballif, and B. Ruhstaller, "Design of Perovskite/Crystalline-Silicon Tandem Solar Cells," in *32nd European Photovoltaic Solar Energy Conference and Exhibition* (2016), pp. 1276–1279.
12. T. Lanz, B. Ruhstaller, C. Battaglia, and C. Ballif, "Extended light scattering model incorporating coherence for thin-film silicon solar cells," *J. Appl. Phys.* **110**(3), 033111 (2011).
13. R. Santbergen and R. J. C. van Zolingen, "Modeling the thermal absorption factor of photovoltaic/thermal combi-panels," *Energy Convers. Manage.* **47**(20), 3572–3581 (2006).
14. L. A. Petterson, L. S. Roman, and O. Inganäs, "Modeling photocurrent action spectra of photovoltaic devices based on organic thin films," *J. Appl. Phys.* **86**(1), 487–496 (1999).
15. J. Kang, X. Wang, P. Bermel, and C. Liu, "S4: Stanford Stratified Structure Solver" <https://nanohub.org/resources/s4sim> (2014).
16. SETFOS 4.6 by Fluxim AG, <https://www.fluxim.com/>.
17. B. Lipovšek, A. Čampa, F. Guo, C. J. Brabec, K. Forberich, J. Krč, and M. Topič, "Detailed optical modelling and light-management of thin-film organic solar cells with consideration of small-area effects," *Opt. Express* **25**(4), A176–A190 (2017).
18. J. Werner, C.-H. Weng, A. Walter, L. Fesquet, J. P. Seif, S. De Wolf, B. Niesen, and C. Ballif, "Efficient Monolithic Perovskite/Silicon Tandem Solar Cell with Cell Area >1 cm²," *J. Phys. Chem. Lett.* **7**(1), 161–166 (2016).
19. J. Werner, L. Barraud, A. Walter, M. Bräuninger, F. Sahli, D. Sacchetto, N. Tétreault, B. Paviet-Salomon, S.-J. Moon, C. Allebé, M. Despeisse, S. Nicolay, S. De Wolf, B. Niesen, and C. Ballif, "Efficient Near-Infrared-Transparent Perovskite Solar Cells Enabling Direct Comparison of 4-Terminal and Monolithic Perovskite/Silicon Tandem Cells," *ACS Energy Lett.* **1**(2), 474–480 (2016).
20. J. Escaré, K. Söderström, M. Despeisse, S. Nicolay, C. Battaglia, G. Bugnon, L. Ding, F. Meillaud, F. J. Haug, and C. Ballif, "Geometric light trapping for high efficiency thin film silicon solar cells," *Sol. Energy Mater. Sol. Cells* **98**, 185–190 (2012).
21. P. Löper, M. Stuckelberger, B. Niesen, J. Werner, M. Filipič, S.-J. Moon, J.-H. Yum, M. Topič, S. De Wolf, and C. Ballif, "Complex Refractive Index Spectra of CH₃NH₃PbI₃ Perovskite Thin Films Determined by Spectroscopic Ellipsometry and Spectrophotometry," *J. Phys. Chem. Lett.* **6**(1), 66–71 (2015).
22. M. A. Green, "Self-consistent optical parameters of intrinsic silicon at 300K including temperature coefficients," *Sol. Energy Mater. Sol. Cells* **92**(11), 1305–1310 (2008).
23. Z. C. Holman, M. Filipič, A. Descocudres, S. De Wolf, F. Smole, M. Topič, and C. Ballif, "Infrared light management in high-efficiency silicon heterojunction and rear-passivated solar cells," *J. Appl. Phys.* **113**(1), 013107 (2013).
24. M. Filipič, P. Löper, B. Niesen, S. De Wolf, J. Krč, C. Ballif, and M. Topič, "CH₃NH₃PbI₃ perovskite / silicon tandem solar cells: characterization based optical simulations," *Opt. Express* **23**(7), A263–A278 (2015).
25. H. Hoppe, N. Arnold, N. S. Sariciftci, and D. Meissner, "Modeling the optical absorption within conjugated polymer/fullerene-based bulk-heterojunction organic solar cells," *Sol. Energy Mater. Sol. Cells* **80**(1), 105–113 (2003).
26. M. Morales-Masis, S. Martin De Nicolas, J. Holovsky, S. De Wolf, and C. Ballif, "Low-Temperature High-Mobility Amorphous IZO for Silicon Heterojunction Solar Cells," *IEEE J. Photovoltaics* **5**(5), 1340–1347 (2015).
27. E. Centurioni, "Generalized matrix method for calculation of internal light energy flux in mixed coherent and incoherent multilayers," *Appl. Opt.* **44**(35), 7532–7539 (2005).
28. T. Stuebinger, "Optische Modellierung und Charakterisierung von organischen Donor-Akzeptor-Solarzellen," Bayreuth (2005).
29. K. Jäger, L. Korte, B. Rech, and S. Albrecht, "Numerical optical optimization of monolithic planar perovskite-silicon tandem solar cells with regular and inverted device architectures," *Opt. Express* **25**(12), A473–A482 (2017).
30. J. Werner, G. Nogay, F. Sahli, T. C. J. Yang, M. Bräuninger, G. Christmann, A. Walter, B. A. Kamino, P. Fiala, P. Löper, S. Nicolay, Q. Jeangros, B. Niesen, and C. Ballif, "Complex Refractive Indices of Cesium-Formamidinium-Based Mixed-Halide Perovskites with Optical Band Gaps from 1.5 to 1.8 eV," *ACS Energy Lett.* **3**(3), 742–747 (2018).
31. K. Jäger, M. Fischer, R. A. C. M. M. Van Swaaij, and M. Zeman, "A scattering model for nano-textured interfaces and its application in opto-electrical simulations of thin-film silicon solar cells," *J. Appl. Phys.* **111**(8), 083108 (2012).

32. J.-P. Correa-Baena, W. Tress, K. Domanski, E. H. Anaraki, S.-H. Turren-Cruz, B. Roose, P. P. Boix, M. Grätzel, M. Saliba, A. Abate, and A. Hagfeldt, "Identifying and suppressing interfacial recombination to achieve high open-circuit voltage in perovskite solar cells," *Energy Environ. Sci.* **10**(5), 1207–1212 (2017).

1. Introduction

While the power conversion efficiency of silicon heterojunction solar cells has surpassed 26% [1], a novel route to high-efficiency wafer-based solar cells is being pursued with perovskite/silicon tandems [2], with monolithic devices having reached 23.6% [3] and 4-terminal configurations exceeding 26% [4, 5] with potential to come close to an efficiency of 30%. One of the key points, for this approach to be successful, is to be able to optimize the optical absorption in the active layers namely the perovskite layer and silicon wafer while minimizing parasitic absorption in charge transport layers. Optical simulations have shown to be of tremendous help in this task [6–11]. However, state-of-the-art devices usually combine thick incoherent layers, thin coherent layers and scattering structures, making the optical simulation challenging. Therefore only very few studies simulating state-of-the-art tandem devices have been published so far [7, 8]. Moreover, most of these studies are usually lacking comparisons with experimental studies.

In this context we introduce a simulation tool that combines a 3D ray-tracing algorithm, a net radiation algorithm [12, 13] and thin-film optics using a one-dimensional transfer matrix algorithm (S-matrix) [14], (a generalized version of this algorithm, which can also simulate the impact of periodic structures using rigorous coupled wave analysis, can be found in [15]) to study light interaction with coated layers on planar and textured silicon wafers, as can be found in high-efficiency silicon heterojunction (SHJ) solar cells. This simulation approach has been implemented in our commercial software SETFOS 4.6 [16]. The algorithm is versatile enough to be able to simulate the innovative device configuration where the perovskite sub-cell is conformally deposited on a textured silicon wafer.

We aim to use our simulation tool to simulate and evaluate the potential of perovskite/silicon monolithic tandem solar cells with advanced architectures in order to give guidelines for future device optimization.

Therefore, we compare monolithic tandem solar cells in rear and front-emitter configuration, as well as the impact of introducing surface texturisation on the front, rear and/or intermediate contacts. In these devices, the main constraint for an optical optimization is the matching of photo-generated currents in both sub-cells. In order to improve the validity of our predictions, the simulations were based on experimental data. Moreover, in a final section we will evaluate the potential of cesium-formamidinium-based perovskite materials with varied bandgaps leading to a change of the absorption spectrum and of the open-circuit voltage (V_{oc}).

2. Simulation approach

As mentioned in the introduction, the multi-scale optical model that will be used combines a ray tracing algorithm, a thin-film optics solver and a net-radiation algorithm [12, 13] which connects the optical fluxes at each interface of the multi-layer structure, therefore taking into account multiple reflection and transmission events. For the sake of readability the key elements of the net-radiation algorithm developed by Lanz et al. [12] are repeated below.

In incoherent layers and at the interface between two incoherent layers, only the intensity distribution of the light is taken into account. For a given wavelength of light, at each interface i the distribution of light incident from the top (index a) or from the bottom (index c) can be described by a vector (q) with a length equal to the number of discretized angles considered in the simulation. The same is true for the light travelling away from the interface in the top (index b) and bottom layer (index d). The equations below connect the light fluxes at the interface i :

$$q_{i,a} = \tau_{i-1} \times q_{i-1,d} \quad (1)$$

$$q_{i,b} = r_{i,+} \times q_{i,a} + t_{i,-} \times q_{i,c} \quad (2)$$

$$q_{i,c} = \tau_i \times q_{i+1,b} \quad (3)$$

$$q_{i,d} = r_{i,-} \times q_{i,c} + t_{i,+} \times q_{i,a} \quad (4)$$

In the equations above, $r_{i,+/-}$ represents the interface reflection for light incident from the top/bottom side, $t_{i,+/-}$ represents the interface transmission for light incident from the top to the bottom or from the bottom to the top, respectively. Finally, τ_i represents light transmission in layer i possibly experiencing absorption between the interfaces i and $i + 1$.

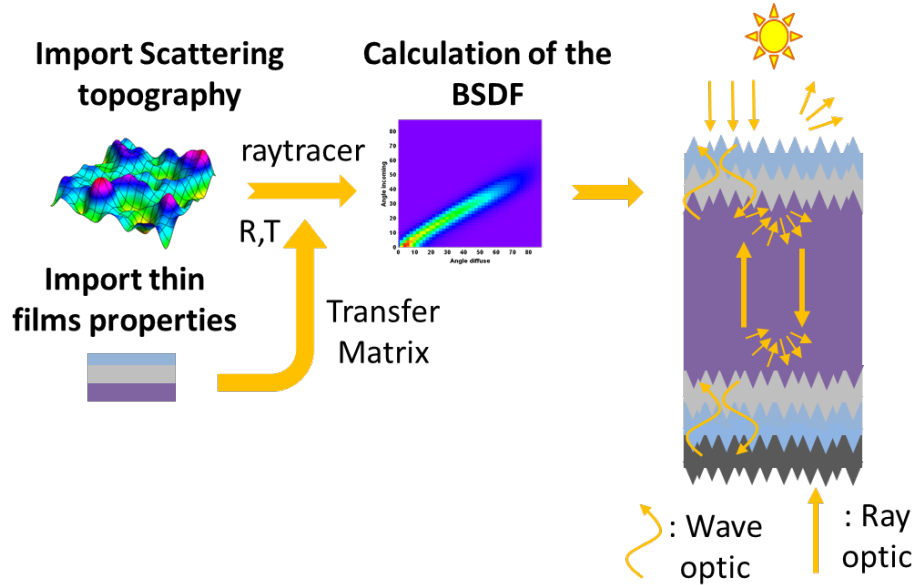


Fig. 1. Schematic representation of the modelling workflow included in SETFOS 4.6 for the simulation of solar cells featuring textured interfaces with optional thin film coatings.

In the particular case where the interface i is flat, the reflection and transmission are simply calculated using the Snell and Fresnel's law. In the more general case of the microtexture e.g. present on the random etched silicon wafer surface considered here, the reflection and transmission properties (also called BSDF: Bi-directional scattering distribution function) are calculated using a ray-tracing algorithm prior to running the net radiation algorithm. Figure 1 summarizes the simulation workflow.

A similar simulation approach was developed in [17] to simulate the impact of light management structure in the absorption of the thin film stack by combining a raytracing algorithm with a thin film simulator. The main difference with the approach described here is that the multiple reflection-transmission events are tackled by a raytracing algorithm whereas this is taken into account in the net radiation algorithm here. The main advantage of the net-radiation algorithm is that it only consists of a linear system of equation that can be solved very efficiently compared to the ray-tracing algorithm which relies on Monte-Carlo simulations. Therefore in order to save simulation time, in our approach, the raytracing algorithm is only run at the beginning of the simulation to calculate the BSDFs of the different textured interfaces.

For one of the tandem cell structures investigated in this work the microtexture interface is actually a coated interface meaning that thin optically coherent layers are conformally deposited on top of the random rough texture. In this latter case, a transfer matrix algorithm for thin film optics is run to calculate the reflection and transmission coefficients of the thin

film coating in a first stage. These coefficients are then considered in the ray-tracing algorithm to calculate the reflection and transmission scattering distribution of the interface for all incoming angles between 0 and 90 °. The optical model also calculates the spectral light absorbance in all coherent and incoherent layers.

3. Comparison with experimental results

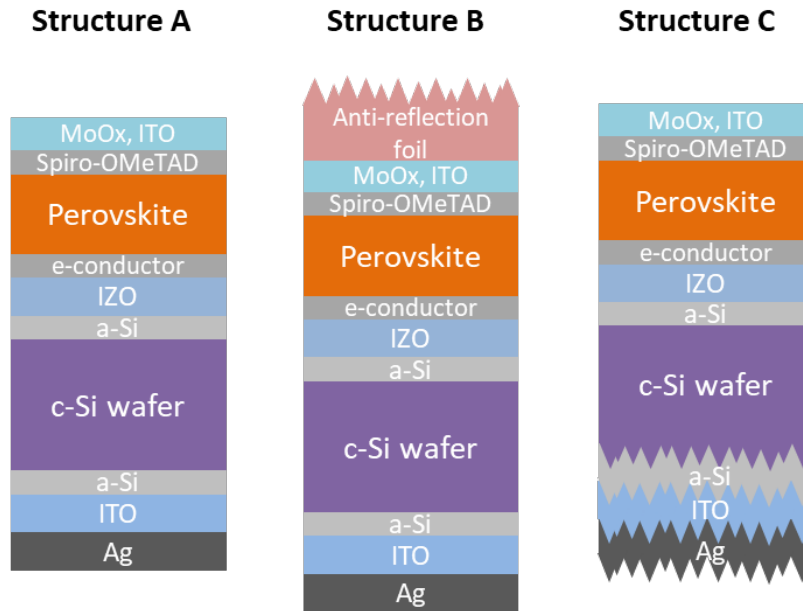


Fig. 2. Cross-section schematics of the perovskite/silicon tandem cells used to compare simulation results with published experimental data: Structure A: monolithic tandem with double-side polished (DSP) silicon bottom cell; Structure B: Structure B with a microtextured anti-reflective foil at the front; Structure C: monolithic tandem with rear-side textured silicon bottom cell.

For validation, our optical simulation model was compared to previously published results of perovskite/silicon monolithic tandem cells. In this first part of the manuscript, we focus on tandem cells using a methylammonium lead iodide (MALI) perovskite top cell in the *n-i-p* configuration where the p-doped side is facing the illumination. Scattering interfaces have been introduced at different locations in the device, namely by means of a microtextured antireflection foil at the front or as a texture at the rear of the silicon wafer as shown in Fig. 2.

The layer sequence considered here is the same as presented by Werner et al. [18, 19]: ITO (110nm), MoOx (10nm), Spiro-OMeTAD (183nm/190nm), perovskite (345 nm/285nm), PCBM (20nm), IZO (40 nm), a-Si (15 nm), silicon (280 um), a-Si (15 nm), ITO (120 nm), silver. For the Spiro-OMeTAD and the perovskite layers, 2 different layer thicknesses were used, as two different devices were studied in [18] and [19] and simulated in this contribution. The exact thickness of the Spiro-OMeTAD and the perovskite layers was obtained by fitting the measured external quantum efficiency (EQE) spectra to the simulated absorbance spectra of the flat devices. These values were kept constant when simulating the corresponding devices with scattering structures.

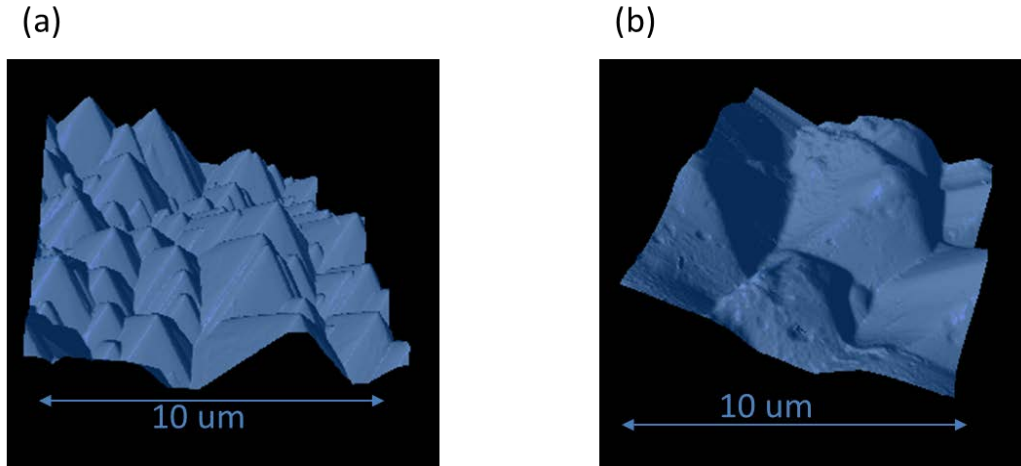


Fig. 3. Topography measurement by AFM of the textured silicon wafer (a) and of the ARF foil (b).

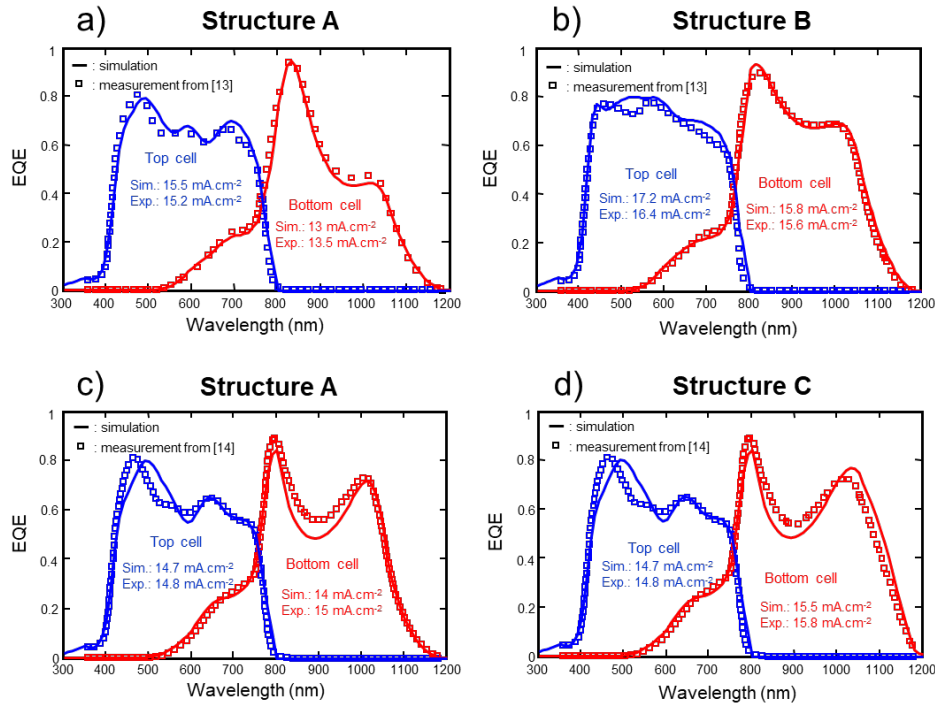


Fig. 4. Comparison between measured and simulated EQE spectra for different perovskite silicon tandem structures: device structure a from Fig. 2 in (a) and (c), device b from Fig. 2 in (b) and device c from Fig. 2 in (d). In (a) and (b), the Spiro-OMeTAD layer thickness was set to 183 nm and the perovskite layer thickness was set to 345 nm. In (c) and (d), the Spiro-OMeTAD layer thickness was set to 190 nm and the perovskite layer thickness was set to 285 nm.

In case of the structure C in Fig. 2, the rough texturing of the silicon was achieved by chemical etching. The topography of this textured surface was measured by atomic force microscopy (AFM), as shown in Fig. 3(a), and then imported in SETFOS for the simulation.

In case of structure B of Fig. 2, the microtextured antireflective foil was fabricated by embossing the textured silicon wafer onto a PET foil [20]. Again the textured foil was measured by AFM [Fig. 3(b)] and imported in SETFOS to calculate the corresponding BSDF as illustrated in Fig. 1.

It is noteworthy that the rear side of the structure C in Fig. 2 represents the case of a ‘coated texture interface’ discussed in the first part of this contribution: indeed the thin ITO and silver layers are both conformally coated on the rough silicon wafer on the rear side of the device.

In Fig. 4 we show the comparison of measured sub-cell EQE spectra with simulated layer absorbance spectra of the perovskite layer and the crystalline silicon wafer, respectively. The refractive index dispersion of the perovskite was taken from Löper et al. [21] (also shown further below) while the refractive index dispersion of silicon was taken from [22]. The refractive indices of ITO, MoO₃, Spiro-OMeTAD, PCBM, IZO and amorphous silicon were taken from [16, 23–27]. We have assumed that all the layers made of amorphous silicon had the same optical index whether they are p-doped, n-doped or intrinsic. We find a fairly good agreement between the simulated absorption and the measured EQE from [18, 19] in Fig. 4 for the three cases defined in Fig. 2. Please note that a constant internal quantum efficiency (IQE) of 0.95 was assumed for the perovskite sub-cell in the simulations.

As can be seen in Figs. 4(c) and 4(d), when the rear side of the silicon wafer is textured using an etching process, only the absorption in the near infrared spectral range is improved in the silicon sub-cell. This trend is nicely reproduced in the simulations.

However, the agreement between simulations and experiments is not perfect and sample to sample variations with respect to nominal layer thicknesses are preventing detailed comparisons. For example, the EQE in Figs. 4(a) and 4(c) differ as the two devices were fabricated few months apart and the processing conditions were slightly changed. Therefore these two flat devices showed somewhat different characteristics. It can also be noticed in Figs. 4(c) and 4(d) that the simulations overestimate interference effects in the bottom cell, a possible reason could be that the intrinsic roughness of the perovskite layer and more generally non-uniformities of the different layers, were neglected in these simulations. However, the overall trend on the experimental EQE spectra can nicely be reproduced by simulation in both the perovskite and the silicon sub-cells for the different devices. This confirms the validity of the modeling approach implemented in SETFOS and presented here.

4. Evaluation of potential device architectures

As the comparison with experimental results shown above revealed a good agreement with simulation results, the optical simulator SETFOS was used to quantify the potential of different device architectures. We identified in the previous section that an IQE of 0.95 can nicely reproduce the measured EQE of the perovskite layer, therefore this value was kept at this value in order to simulate the photo-generated current (an IQE equal to 1 was assumed for the silicon sub-cell).

4.1 Inverted structure versus standard architecture

In order to reduce parasitic absorption due to the presence of Spiro-OMeTAD, recently, a *p-i-n* device architecture has been proposed, where, the n-side of the device is facing the illumination instead of the p-side (see right side in Fig. 5). Of course, with this approach, the layer sequence in the silicon sub-cell also needs to be inverted. The advantage of this architecture is that the hole transport layer of the perovskite sub-cell is positioned below the perovskite layer, allowing the use of thin n-type materials on top of the device and therefore reducing parasitic absorption. A record efficiency of 23.6% for monolithic tandem architecture has been achieved using this approach [3].

In order to compare both device polarities, optical simulations were performed for tandem cells featuring a polished front and textured rear silicon interface. A scattering anti-reflection

foil, as shown in the previous section was assumed to be applied on the top of the structure. The following device structure was considered for the tandem cell in the $p-i-n$ configuration [Fig. 5(b)]: anti-reflection foil, ITO (110nm), SnO_2 (9nm), C_{60} (15nm), Perovskite (optimized), NiO (20nm), ITO (40nm), a-Si (24nm), Si (280um), a-Si (24nm), ITO (80nm), Silver. For the simulation, the refractive indices of C_{60} and NiO were taken from [28] and [16].

Concerning the standard $n-i-p$ architecture, the layer sequence which was used for the simulation is the same as the one described in the section above [Fig. 5(a)]: anti-reflection foil, ITO (110nm), MoO_3 (10nm), Spiro-OMeTAD (optimized), Perovskite (optimized), PCBM (20nm), IZO (40 nm), a-Si (15 nm), Silicon (280 um), a-Si (15 nm), ITO (120 nm), Silver.

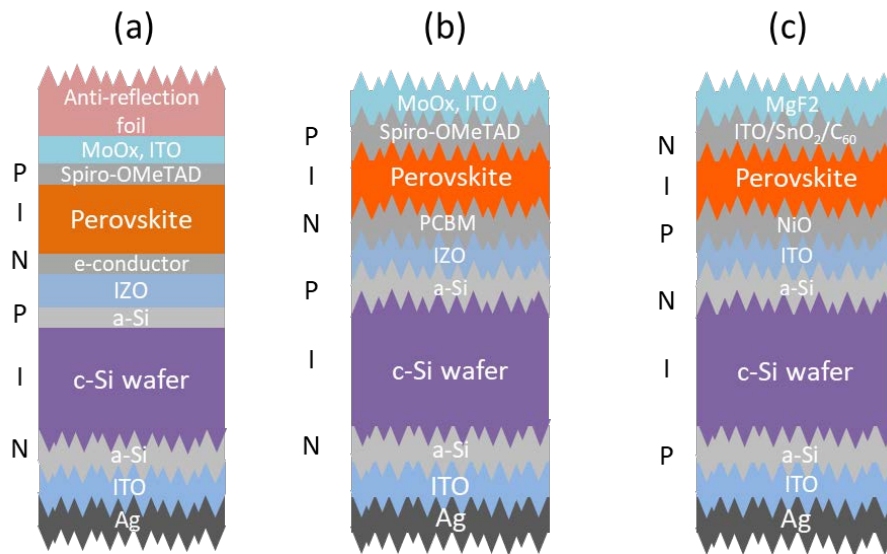


Fig. 5. Schematic illustration of the devices used to compare the $n-i-p$ (a) and $p-i-n$ architecture (b), and to compare with the conformal deposition of the perovskite sub-cell on top of a textured silicon wafer (c).

In order to obtain a fair comparison of both architectures, devices were optically optimized in order to achieve the highest photocurrent in both sub-cells at current-matching conditions. For the $n-i-p$ architecture the thickness of the Spiro-OMeTAD and perovskite layers was varied in order to achieve the highest efficiency. As for the $p-i-n$ configuration, only the perovskite layer was optimized. The simulation results shown in Fig. 6 confirm the expected results: using a $p-i-n$ architecture, the maximum photocurrent at current matching condition is found to be higher by almost 2 mA/cm² in the inverted structure compared to the $n-i-p$ architecture using Spiro-OMeTAD in the front.

In case of the $n-i-p$ architecture, the maximum device efficiency was achieved for a perovskite layer thickness of 320 nm and a Spiro-OMeTAD thickness of 130 nm leading to a photo-generated current of 17.0 mA/cm². This layer thickness for the Spiro-OMeTAD represents the experimentally determined lower limit for obtaining a device with sufficient electrical performance; usually thicker Spiro-OMeTAD films are used leading to more parasitic absorption in this layer. As for the $p-i-n$ structure the maximum efficiency was achieved for a perovskite layer thickness of 400 nm with a maximum photo-current of 18.9 mA/cm². This increase by almost 2 mA/cm² is remarkable and corresponds to a relative increase by approximately 11%. However, other $n-i-p$ cell layer stacks could in principle also work with much thinner and undoped layers, but with the current materials available for state-

of-the-art cells, the *p-i-n* configuration is optically better as all the transport layers are thin and undoped or weakly doped.

It can be noticed in Fig. 6 that even in the inverted structure some residual absorption appears in the ETL (C_{60}) layer deposited on-top of the perovskite, however this absorption remains small and could be decreased further by using a thinner C_{60} layer on a perovskite layer with low surface roughness. Moreover, it is interesting to notice that optical interferences seem to have less impact for the *p-i-n* device structure, this latter point was also recently reported in [21], and is the consequence of thick HTL layer used in the *n-i-p* structure.

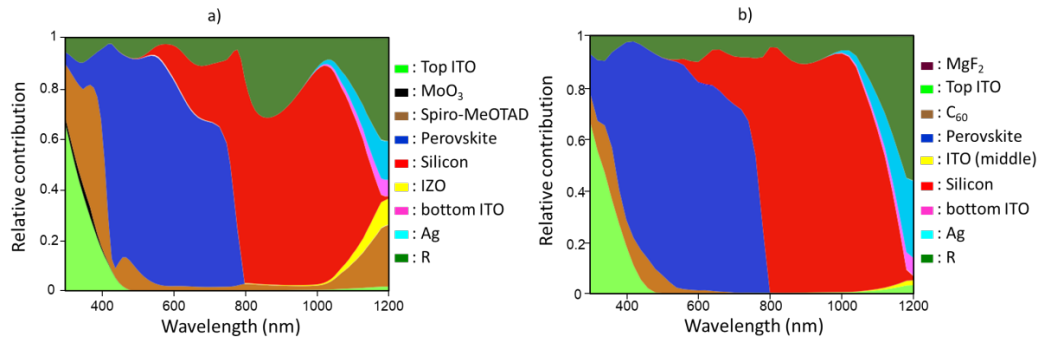


Fig. 6. Absorbance of the main absorbing layers of the perovskite-silicon tandem solar cell at maximum current matching conditions for the *n-i-p* architecture (a) and the *p-i-n* one (b). The R represents the reflectance of the device.

4.2 Scattering foil versus conformal coating

Santbergen et al. [8] showed that the configuration where the perovskite layer is conformally deposited on top of a textured silicon wafer [Fig. 5(c)] is the most promising structure in order to maximize the light absorption in both the perovskite and silicon sub-cells for *n-i-p* structures. Such a conformal coating of the perovskite cell has yet to be experimentally demonstrated, currently set back by its incompatibility with the solution processing techniques commonly used in the perovskite field. In this section we have optically optimized *p-i-n* device, using charge transport layers and electrode materials that can be deposited with physical or chemical vapor deposition-based conformal techniques. The device layer stack considered here is the following: anti-reflection MgF_2 layer (optimized), ITO (110nm), SnO_2 (9nm), C_{60} (15nm), Perovskite (optimized), NiO (20nm), ITO (40nm), a-Si (24nm), Si (280um), a-Si (24nm), ITO (80nm), Silver.

Using this architecture, the reflection losses can be strongly reduced (as shown in Fig. 7), a maximum photocurrent of $19.6 \text{ mA}\cdot\text{cm}^{-2}$ could be achieved, which represents $0.7 \text{ mA}\cdot\text{cm}^{-2}$ more than using the scattering foil. This maximum was achieved for a MgF_2 layer thickness equal to 110 nm and a perovskite layer thickness equal to 440 nm.

Therefore, we can conclude, from this section, that the *p-i-n* architecture where the perovskite layer is conformally deposited on top of a textured silicon substrate represents the most promising architecture, which was thus kept for the following section.

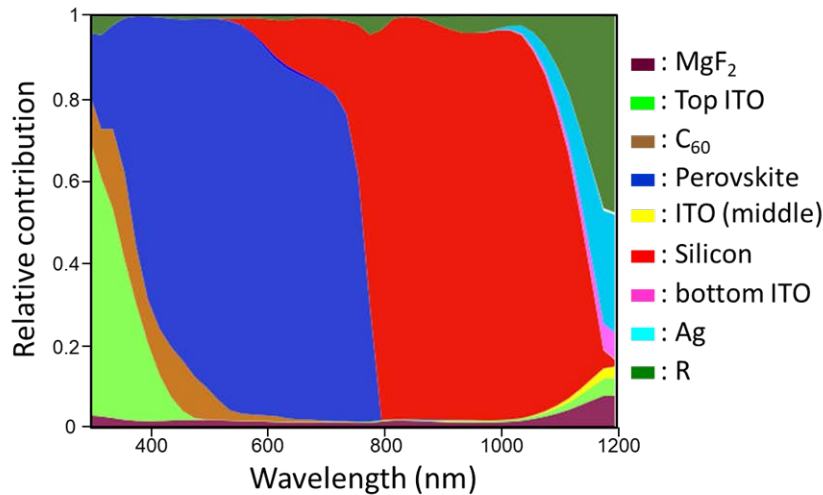


Fig. 7. Absorbance of the main absorbing layers of the *p-i-n* perovskite-silicon tandem solar cell, where the perovskite sub-cell is conformally deposited on top of a textured silicon wafer [Fig. 5(c)]. The R represents the reflectance of the device.

4.3 Variation of the perovskite bandgap

In order to further improve the efficiency of tandem perovskite/silicon solar cells, perovskite materials with higher bandgaps can be used to decrease the energy loss by thermalization of photo-carriers in the perovskite layer and therefore to achieve a higher V_{oc} for the full device [29]. As the photocurrent in the top cell decreases with increasing bandgap, optimizing the overall tandem performance involves a trade-off between reaching matched sub-cell photocurrents and maximizing V_{oc} .

In this section, the potential of different perovskite materials will be evaluated based on a combination of experimental results and simulations. To this aim, perovskite materials based on CsxFA1-xPbI3-xBrx with bandgaps of ~ 1.6 eV and ~ 1.7 eV were synthesized. The refractive indices of these layers were characterized by variable angle spectroscopic ellipsometry to be used later in the optical simulations and can be found in [30].

As shown in the previous sections, the *p-i-n* structure with a conformal deposition of the perovskite cell on top of a textured silicon substrate appears to be the device structure with the highest photocurrent potential, therefore this architecture was considered for optical simulations with these alternative perovskite materials. Again, devices were optically optimized in order to achieve the current matching condition

The maximum value for matched currents for the 1.6 eV CsxFA1-xPbI3-xBrx and for the MALI perovskite (bandgap around 1.55 eV), was found equal to 19.6 mA/cm^2 in both cases assuming an IQE equal to 0.95. A maximum current of 20.2 mA/cm^2 can be achieved for the 1.6 eV material in case the IQE can be increased to 1. Moreover, in a real device interference effects are likely to be reduced thanks to the perovskite intrinsic roughness and more generally due to layer non-uniformities, which could lead to a reduction of the reflectance and therefore to an additional increase of the maximum photo-generated current, in line with the observation that interference effects in the bottom cell current tend to be more pronounced than for the experimental data [Figs. 4(c) and 4(d)].

The perovskite layer thickness maximizing the matched sub-cell current value was found equal to 440 nm for the MALI and 780 nm for the 1.6 eV perovskite. In Fig. 8 we show the absorbance in the different layers of tandem cells with the 1.6 eV or the 1.7 eV perovskite layer, as well as the total reflectance per wavelength. Due to the higher bandgap, the absorbance edge of the 1.7 eV material is shifted to lower wavelength, such that the top cell

photocurrent is limited due to the high absorptance of the front C_{60} and ITO layers at short wavelengths. Therefore, it was not possible to achieve a current matching condition for the perovskite material with a bandgap of 1.7 eV. Only a maximum photocurrent of 18.1 mA/cm² was achieved for a perovskite thickness of 1000 nm.

However, if parasitic absorption in the blue could be reduced, perovskite materials with a higher bandgap can still be promising, with an optimal value of ~1.72 eV for ideal tandem cells without parasitic absorption losses [31].

From these simulations we conclude that the perovskite material with a bandgap of 1.6 eV is promising for the tandem architecture studied in this contribution, as matched sub-cell currents can be reached with reasonable layer thicknesses and the perovskite bandgap of 1.6 eV is likely to give a higher V_{oc} than that of MALI, with an optimum probably lying around 1.65 eV considering the parasitic absorption of the different layers. Assuming a V_{oc} of the perovskite cell equal to 1.1 V, an IQE equal to 1, a fill factor of 80% for both the silicon and the perovskite sub-cells and a V_{oc} of the silicon cell equal to 0.7 V, would lead to an overall device efficiency slightly above 29%. An efficiency of 31% can be achieved in case the V_{oc} of the perovskite layer can be increased toward 1.2V as can be expected and which was already achieved for similar perovskite materials on single junction-solution cells [32].

However, the deposition of a 780 nm thick film for current matching without affecting the electrical cell performance may represent a challenge. Similarly, the conformal deposition of the perovskite solar cell layers on the front texture of the silicon wafer has yet to be achieved and reported in sufficiently high quality.

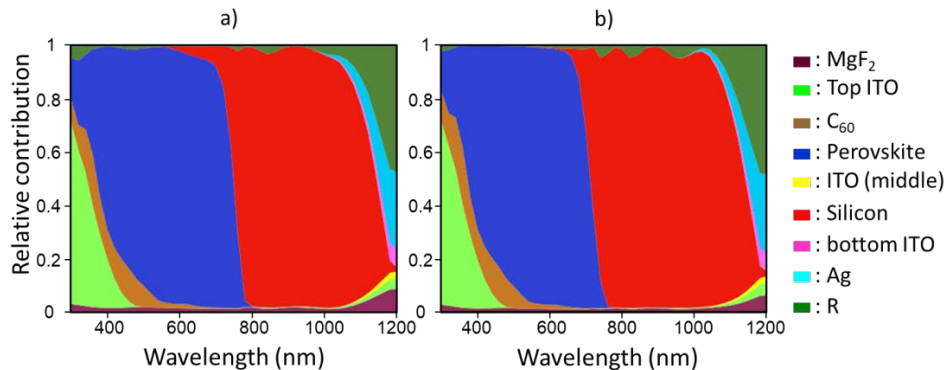


Fig. 8. Absorbance of the main absorbing layers of the solar cell at maximum current matching conditions for the perovskite materials with $E_g = 1.6\text{eV}$ (a). In (b) we show the absorbance of the different layers for the 1.7 eV bandgap perovskite cell (no current matching condition was found for this material). For all cases R represents the reflectance

5. Conclusion

In this contribution we have presented an optical model able to simulate state-of-the-art perovskite/silicon tandem solar cells including scattering structures. The simulations based on this model were then compared with experimental results in order to validate our modelling approach and to extract the IQE of the perovskite sub-cell. In a next step, this simulation tool was used to investigate the potential of different monolithic device architectures and exploiting rear- as well as front-side textures for improved light harvesting. By comparison of the most commonly used $n-i-p$ layer stack with spiro-OMeTAD and a state-of-the-art $p-i-n$ layer stack with C_{60} at the front, we found that the latter was giving a better optical performance for flat devices and when considering front- and rear-side light scattering. Finally, cesium-formamidinium-based perovskite materials with varied bandgap were synthesized and optically characterized and their potential in a tandem device was assessed quantitatively by optical solar cell simulations. It was identified that, among the tested

perovskite materials including MAPbI_3 and $\text{CsFAPbI}_{3-x}\text{Br}_x$ with band gaps of 1.6 and 1.7 eV, the one having a bandgap of 1.6 eV was the most promising with a potential of reaching a power conversion efficiency of 31%. In order to achieve higher efficiencies using materials with wider bandgaps, further investigations will be needed to develop thick high-quality perovskite films, that can be conformally deposited on silicon pyramids and to reduce all parasitic absorption losses in the front electrode particularly in the blue spectral region.